Phase estimation at the point-ahead angle for AO pre-compensated ground to GEO satellite telecoms

Perrine Lognoné, Jean-Marc Conan, Ghaya Rekaya, Nicolas Védrenne

Research Article Vol. 31, No. 3 / 30 Jan 2023 / Optics Express 3441
Optics EXPRESS

Phase estimation at the point-ahead angle for AO pre-compensated ground to GEO satellite telecoms

PERRINE LOGNONÉ,[1,2,*] JEAN-MARC CONAN,[1] GHAYA REKAYA,[2] AND NICOLAS VÉDRENNE[1]

[1]ONERA, DOTA, Paris Saclay University, 92322 Châtillon, France
[2]Télécom Paris, 91120 Palaiseau, France
[*]perrine.lognone@onera.fr

Abstract: We present a new method to estimate the off-axis adaptive optics pre-compensation phase of a ground to GEO satellite telecom link suffering from point-ahead anisoplanatism. The proposed phase estimator relies on the downlink phase and log-amplitude measurements that are available at the optical ground station. We introduce the analytical tools, extended from the literature, to build the estimator as well as a general modal formalism to express the reciprocal residual phase covariance matrix resulting from any estimation linear with measurements. We use this residual phase covariance matrix to generate independent coupled flux samples thanks to a pseudo-analytical approach and study the gain offered by the proposed estimator on the coupled flux statistics, in various atmospheric conditions. The estimator is shown to reduce the anisoplanatic residual phase variance by at least 35%, and 46% at best, with a greater impact on the lower modes, especially on the tip and tilt residual phase variances. The phase variance reduction brings a gain up to 15 dB on the cumulative density function at probability 10^{-3}. This gain should allow to relax the power constraints on the link budget at the OGS and renews the interest in large aperture diameter (60 cm class telescopes) for GEO Feeder links by reducing the atmospheric turbulence impact on the uplink coupled signal.

1. Introduction

Optical GEO-Feeder links are foreseen to be a game changer in the telecommunication next generation very high throughput networks [1]. As the space network is envisioned to complement the terrestrial one, high capacitive links are needed to connect the space segment to the ground core network. In this scenario, the GEO satellite acts as a relay node and optical links are a key technology to reach the targeted capacity while overcoming the radio-frequency bottleneck. Unfortunately, today's earth to space optical telecom link performance is limited by cloud coverage and atmospheric turbulence [2]. While optical ground station (OGS) diversity tackles cloud blockage [3], telecom signal distortion due to atmospheric turbulence still needs to be addressed. A solution is to use physical reliability mechanisms, to be deployed on ground, such as multi-aperture diversity [4–6] or adaptive optics (AO) used to pre-compensate the emitted laser beam phase. We focus our analysis on the AO monolithic large aperture solutions for its potential in terms of geometrical losses [7]. One possibility is to pre-compensate by the downlink measured phase [8], so called "classical" method. However, because of the point ahead angle (PAA) inherent to the GEO-Feeder link geometry as depicted in Fig. 1, the downlink and uplink do not propagate through the same turbulent volume. Thus, the classical approach suffers from point-ahead anisoplanatism and is not optimal [8,9]. As a result, the received signal on-board the satellite undergoes long and deep fades.

Several solutions to overcome the anisoplanatic error in ground-to-geostationary satellite telecoms have been reported in the literature. The initial concept of taking advantage of a

#476328 https://doi.org/10.1364/OE.476328
Journal © 2023 Received 23 Sep 2022; revised 30 Nov 2022; accepted 30 Nov 2022; published 17 Jan 2023

Optics EXPRESS

wavefront measurement from a downlink beam at PAA is presented by Tyson [8]. This downlink beam could either come from a slave satellite, a solution whose cost and feasibility still needs to be investigated, or from a laser guide star (LGS). A numerical analysis of the performance of the LGS based pre-compensation can be found in [10]. However, these systems are complex to implement and Tip-Tilt indetermination remains a limitation [10,11].

In the meantime, there is a need to evaluate and compare the telecom performance associated to the different methods. In this aim, because ground to satellite optical data is scarce, a great effort have been put to perform outdoor optical link demonstrations [12–15] and to develop free-space optical (FSO) link numerical models. Two kinds of numerical models are used to simulate AO corrected uplink coupling efficiency in the literature: End-to-end (E2E) and pseudo-analytical models based on link reciprocity. E2E modeling, relying on Monte-Carlo propagation of the optical beam through a turbulent volume discretized in phase screens, are considered as the most accurate simulation tool from the literature [10,16]. However, E2E modeling is computationally intensive, thus, pseudo-analytical approaches have been developed to speed up the computation. They rely on an analytical description of the statistics of the residual phase and amplitude of the field in the OGS pupil, that can be expressed either in a modal [7,17,18] or Fourier formalism [19]. Knowing these statistics, one can draw field samples and compute the coupling efficiency as the numerical overlap integral with a Gaussian mode.

As seen above, the turbulence and field statistics are used to model the coupling efficiency of the uplink coupled signal. These statistics can also be used for phase estimation away from measurement directions. This can be for instance performed with minimum mean square error (MMSE) linear estimation. This approach can be found in astronomy, particularly in Whiteley [20] using the phase measurement from a single beacon and in AO tomographic approaches as in [21,22] and references therein, using several guide star phase measurements to perform the estimation. This MMSE method has the advantage to only use the information already available at the OGS. Both techniques use the MMSE estimation to minimize the wavefront error given phase measurements and statistical priors.

In this article, we propose to apply the MMSE estimation of Whiteley [20] to the telecom wavefront estimation at PAA. Furthermore, we extend this work and propose a new phase estimator based on phase and log-amplitude on-axis measurements and associated statistical priors. While the phase information is classically used to perform the AO correction, the log-amplitude is usually discarded whilst being freely available from the wavefront sensor measurements at the OGS. We compute the estimator thanks to analytical modal covariance matrices. This formalism also allows to extend the pseudo-analytical performance assessment tools to the general case of a phase estimation linear with respect to the measurements. Thanks to this tool, we evaluate the gain brought by the new estimator in terms of both residual phase variance and coupled signal statistics, with respect to state of the art methods. We also study the gain sensitivity to various atmospheric conditions.

In section 2 we present the reciprocal bidirectional system and the pseudo-analytical model to compute the coupling efficiency relying on the general phase modal covariance matrix formalism. Section 3 is dedicated to the MMSE method and the new estimator relying on the phase and log-amplitude downlink measurement vector and associated statistical priors. Tools needed to compute the said estimator are also presented. Finally, we assess in section 4 the new estimator gain on the coupled flux statistics thanks to the pseudo-analytical simulation, with respect to state of the art methods.

Optics EXPRESS

2. AO pre-compensated uplink modeling

2.1. Notations

Vectors and matrices will be denoted by bold lowercase and uppercase variables. The term denoted j corresponds to the imaginary unit. The scalar product weighted by W is defined as :

$$\langle \mathrm{X}|\mathrm{Y}\rangle_{\mathrm{W}} \triangleq \iint \mathrm{W}(\mathbf{r})\mathrm{X}(\mathbf{r})\mathrm{Y}^{*}(\mathbf{r})\mathrm{d}^{2}\mathbf{r}, \tag{1}$$

where $\mathrm{X}(\mathbf{r})$, $\mathrm{Y}(\mathbf{r})$ and $\mathrm{W}(\mathbf{r}) \in \mathbb{C}$ are functions of the spatial coordinates, $\mathrm{Y}^{*}(\mathbf{r})$ denotes the complex conjugate of $\mathrm{Y}(\mathbf{r})$.

Now, let $\mathbf{X}$ and $\mathbf{Y}$ be two random vectors $\in \mathbb{R}^{\mathrm{Nx1}}$. They depict two physical quantities that can be of same or different nature, and either issued from the same optical path or from optical paths separated by an angle $\Delta\alpha$. We define the cross-covariance matrix between $\mathbf{X}$ and $\mathbf{Y}$, and the covariance matrix if Y=X, as:

$$\mathbf{\Gamma_{XX}}(0) \triangleq \mathbb{E}[(\mathbf{X}-\mathbb{E}[\mathbf{X}])\,(\mathbf{X}-\mathbb{E}[\mathbf{X}])^{\mathrm{T}}] = (\mathbb{E}[\mathrm{x_i x_k}] - \mathbb{E}[\mathrm{x_i}]\mathbb{E}[\mathrm{x_k}])_{\mathrm{i_0 \le i,k \le i_N}} \tag{2}$$

$$\mathbf{\Gamma_{XY}}(\Delta\alpha) \triangleq \mathbb{E}[(\mathbf{X}-\mathbb{E}[\mathbf{X}])\,(\mathbf{Y}-\mathbb{E}[\mathbf{Y}])^{\mathrm{T}}] = \left(\mathbb{E}[\mathrm{x_i^0 y_k^{\alpha}}] - \mathbb{E}[\mathrm{x_i^0}]\mathbb{E}[\mathrm{y_k^{\alpha}}]\right)_{\mathrm{i_0 \le i \le i_N, k_0 \le k \le k_N}} \tag{3}$$

where $\mathrm{i_0}, \mathrm{k_0}$ and $\mathrm{i_N}, \mathrm{k_N}$ are the indexes of the first and last elements of X and Y respectively.

2.2. Bidirectional link definition

The considered GEO-Feeder system is a bidirectional optical link between the GEO satellite and the ground. An AO system at the OGS corrects the phase of the incident downlink field before single mode fiber (SMF) injection and pre-compensates the emitted uplink laser mode. Through all the modeling steps, we choose to exploit the reciprocity principle to express wavefront perturbations experienced in the point ahead direction in the OGS pupil and the associated coupled flux, as in [7,19,23–25]. This principle states that the uplink coupling of the emitted mode from the ground after propagation to the satellite receiver mode is equal to the coupling of this receiver mode back-propagated towards the OGS to the station emission mode. Using the reciprocal uplink, as represented in red in the Fig. 2, we can therefore express the off-axis wavefront perturbations and thus analyse the AO pre-compensation performance. We define the complex field after propagation from the satellite to the OGS pupil plane as:

$$\Psi(\mathbf{r}, \mathrm{t}; \alpha) \triangleq \mathrm{A_0} \exp\left(\chi(\mathbf{r}, \mathrm{t}; \alpha) + \mathrm{j}\Phi(\mathbf{r}, \mathrm{t}; \alpha)\right), \tag{4}$$

where χ are the log-amplitude fluctuations, $\mathrm{A_0}$ is the intensity constant term, Φ is the perturbed phase, $\mathbf{r}$ is the space coordinate vector defined over the telescope circular aperture of radius $\mathrm{R_{tel}}$, associated to the aperture transmission function P(r), t is the time and α is the angular direction of the optical path considered. The downlink beam axis is taken as the angular reference α=0, thus, the reciprocal uplink is located at α=PAA as shown in Fig. 2. In this study, we consider a statistical approach and do not study the temporal dynamic of the coupled signal but only the capacity to angularly predict the performance, t is then fixed.

2.3. Choice of a representation basis: Zernike polynomial basis

We use a modal formalism to describe the field phase and log-amplitude, choosing the Zernike polynomial basis. The Zernike is a basis whose polynomial are orthogonal over circular aperture for the scalar product defined over the telescope aperture P(r). It is classical in the AO field to represent the phase on this basis [26], however, it is less common to do likewise concerning the log-amplitude. Yet, this log-amplitude modal expansion has already been used in [27]. We note that other basis could be used to describe these quantities as the zonal basis, or the Fourier basis.

Optics EXPRESS

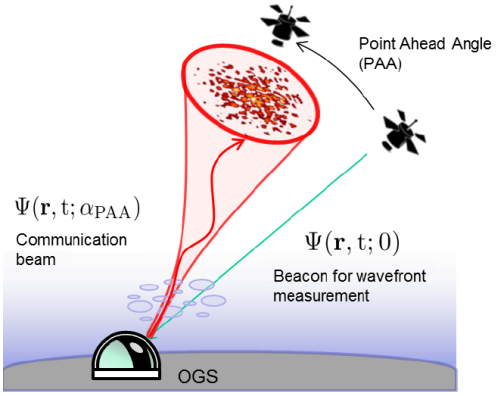

Fig. 1. Sketch of a GEO-Feeder bidirectional link geometry for a given PAA.

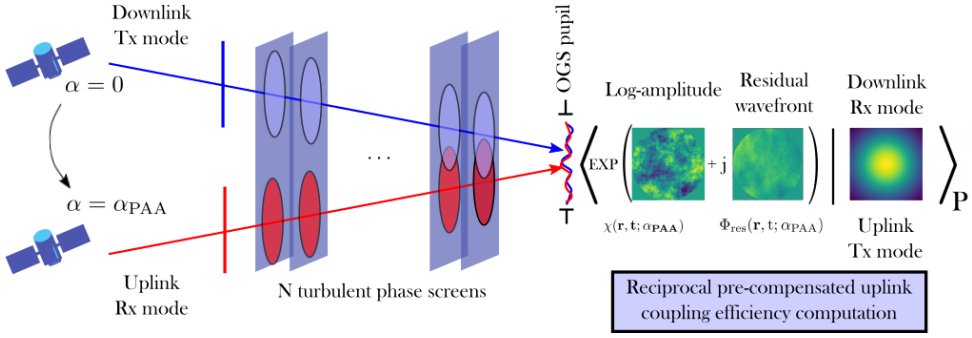

Fig. 2. Scheme of the reciprocal modeling of the GEO-Feeder bidirectional link.

Therefore, the phase and log-amplitude are expanded onto a Zernike polynomial basis subset until the order N_{max} defined by the last polynomial used in the representation. The dimension of this subset is $N_{max} - 1$ for the phase (the first mode, the piston, is not represented as it is not measured by the AO system and do not impact the coupling in a direct detection scheme), and N_{max} for the log-amplitude. Thus, we can write $\Phi(\mathbf{r}; \alpha) = \sum_{i=2}^{N_{max}} a_i^{\alpha} Z_i(\mathbf{r})$ and $\chi(\mathbf{r}; \alpha) = \sum_{i=1}^{N_{max}} b_i^{\alpha} Z_i(\mathbf{r})$ where N_{max} is the number of polynomials used in the representation, $Z_i(\mathbf{r})$ the Zernike polynomial, i its Noll index. We define a second subset, denoted AO, corresponding to the number of modes measured by the AO system from mode 2 and 1 to N_{AO} for phase and log-amplitude, respectively.

Consequently, at a given angle α, these quantities can be depicted by the two following vectors:

$$\mathbf{\Phi}_{\alpha} = \left(a_2^{\alpha} \quad \dots \quad a_{N_{AO}}^{\alpha} \quad \dots \quad a_{N_{max}}^{\alpha}\right)^T, \qquad \text{with } a_i^{\alpha} = \langle \Phi(\mathbf{r}; \alpha) | Z_i(\mathbf{r}) \rangle_P \tag{5}$$

$$\text{and} \quad \boldsymbol{\chi}_{\boldsymbol{\alpha}} = \left(b_1^{\alpha} \quad \dots \quad b_{N_{AO}}^{\alpha} \quad \dots \quad b_{N_{max}}^{\alpha}\right)^T, \qquad \text{with } b_i^{\alpha} = \langle \chi(\mathbf{r}; \alpha) | Z_i(\mathbf{r}) \rangle_P \tag{6}$$

where P is the circular telescope aperture function.

2.4. Reciprocal uplink residual wavefront and coupled flux

2.4.1. AO residual wavefront

We use a reciprocal formalism to explicit the wavefront perturbations at PAA that are corrected by the AO pre-compensation. This allows to evaluate the AO correction performance by computing

Optics EXPRESS

the reciprocal off-axis residual wavefront:

$$\mathbf{\Phi_{res}} \triangleq \mathbf{\Phi_{PAA}} - \hat{\mathbf{\Phi}}_{\mathbf{PAA}}, \tag{7}$$

the difference between the phase of the back-propagated reception mode of the satellite in the OGS pupil plane $\mathbf{\Phi_{PAA}} \in \mathbb{R}^{N_{max}-1}$ and the AO correction phase $\hat{\mathbf{\Phi}}_{\mathbf{PAA}} \in \mathbb{R}^{N_{max}-1}$, both expressed in the subset of Zernike modes of size N_{max}.

We assume the residual wavefront $\mathbf{\Phi_{res}}$ to be the sum of two error contributions: the anisoplanatism induced by the angular decorrelation of the turbulence which affects only the AO subset of modes and the fitting due to the finite AO correction mode basis impacting the high order modes from $N_{AO}+1$ to N_{max}. As the anisoplanatism is the overriding error of the AO error budget [7], and that we consider an optimal AO system, we neglect the errors induced by the AO system as AO loop temporal error, aliasing or wavefront sensor noise. As a result, we can express the correction phase as:

$$\hat{\mathbf{\Phi}}_{\mathbf{PAA}} \triangleq \begin{pmatrix} \hat{\mathbf{\Phi}}_{\mathbf{AO,PAA}} \\ \mathbf{0} \end{pmatrix}, \tag{8}$$

where $\hat{\mathbf{\Phi}}_{\mathbf{AO,PAA}} \in \mathbb{R}^{N_{AO}-1}$ is the correction phase on the AO modes subset. The zero terms cover the rest of the representation mode subset from $N_{AO}+1$ to N_{max}.

We develop a general formalism relevant to every AO corrections computed as linear operations with AO measurements. In this aim, we assume the correction phase to result from a linear operation between a given reconstructor matrix $\mathbf{R}$ and a measurement vector $\mathbf{y}_m$, from the downlink beam, and propose a new formulation for the correction phase:

$$\hat{\mathbf{\Phi}}_{\mathbf{AO,PAA}} \triangleq \mathbf{R}\mathbf{y}_m. \tag{9}$$

The value and dimensions of $\mathbf{R}$ and $\mathbf{y_m}$ depend on the chosen estimation and correction method. We assume that all measurements are noise free since we are in a high flux regime in telecom scenarii.

Under this formalism, we can describe the statistics of the residual phase and show that its covariance matrix, under the notations of section 2.1, is equal to:

$$\mathbf{\Gamma_{res}} \triangleq \mathbb{E}[\mathbf{\Phi_{res}}\mathbf{\Phi_{res}}^{\mathbf{T}}] = \begin{pmatrix} \mathbf{\Gamma}_{\text{aniso}} = [\mathbf{\Gamma}_{\text{AO,res}}]_{2\leq i,k,\leq N_{AO}} & \mathbf{0} \\ \mathbf{0} & \mathbf{\Gamma}_{\text{fitting}} = [\mathbf{\Gamma}_{\Phi\Phi}(0)]_{N_{AO}+1\leq i,k,\leq N_{max}} \end{pmatrix}, \tag{10}$$

where we neglect the cross-covariances between the corrected and uncorrected modes, supposedly weak. We compute the residual phase covariance matrix as:

$$\mathbf{\Gamma_{AO,res}} = \mathbf{\Gamma}_{\Phi\Phi}(0) - \mathbf{R}\mathbf{\Gamma}_{\Phi y_m}(\alpha_{PAA})^T - \mathbf{\Gamma}_{\Phi y_m}(\alpha_{PAA})\mathbf{R}^T + \mathbf{R}\mathbf{\Gamma}_{y_m y_m}(0)\mathbf{R}^T \tag{11}$$

As an example, we can compute the residual phase covariance matrix of the classical pre-compensation case, where the correction phase is based on the downlink phase measurement located at $\alpha = 0$. In this case, $\mathbf{R} = \mathbf{I}_{N_{AO}-1} \in \mathbb{R}^{N_{AO}-1 \times N_{AO}-1}$ and $\mathbf{y_m} = (\mathbf{\Phi_0}) \in \mathbb{R}^{N_{AO}-1}$. As a result, applying Eq. (11), we obtain in this particular case:

$$\mathbf{\Gamma_{AO,res-classical}} = 2\mathbf{\Gamma_{\Phi\Phi}}(\mathbf{0}) - \mathbf{\Gamma_{\Phi\Phi}}(\alpha_{\mathbf{PAA}}) - \mathbf{\Gamma_{\Phi\Phi}}(\alpha_{\mathbf{PAA}})^{\mathbf{T}}. \tag{12}$$

Finally, the metrics to evaluate the pre-compensation performance are the overall mean square error (MSE) and the modal MSE:

$$\text{MSE} = \text{tr}[\mathbf{\Gamma_{res}}] \quad \text{and} \quad \text{MSE}_i = (\mathbf{\Gamma_{res}})_{i,i}, \tag{13}$$

where tr is the trace operator and i the i^{th} Zernike mode index.

Optics EXPRESS

2.4.2. Reciprocal coupled flux

We express the random coupled flux of the pre-compensated signal aboard the satellite reciprocally as the coupling, in the OGS aperture, between the given complex field back-propagated from the satellite at PAA, corrected by AO, and the uplink emission Gaussian mode [25]:

$$\mathrm{f}_{\mathrm{pre-compensated,OGS}\rightarrow\mathrm{satellite}}(\alpha_{\mathrm{PAA}}) = \mathrm{f}_{\mathrm{compensated,satellite}\rightarrow\mathrm{OGS}}(\alpha_{\mathrm{PAA}}). \tag{14}$$

Here, f is a random variable as we only study the statistics behavior of the coupling.

To express f, we assume Φ and χ of the field independent [28]. Therefore, we can consider separately the phase and log-amplitude contributions to the coupling as:

$$\mathrm{f} = \rho_{\Phi} \cdot \rho_{\chi}. \tag{15}$$

The phase contribution is the result of the overlap integral between the field neglecting the log-amplitude fluctuations and the fiber Gaussian mode $\mathrm{M}_0(\mathbf{r})$ [18]:

$$\rho_{\Phi} = \rho_{\mathrm{compensated,satellite}\rightarrow\mathrm{OGS}} = \left| \frac{\left\langle \mathrm{e}^{\mathrm{j}\Phi_{\mathrm{res}}(\mathbf{r})} | \mathrm{M}_0(\mathbf{r}) \right\rangle_{\mathrm{P}}}{\sqrt{\left\langle \mathrm{e}^{\mathrm{j}\Phi_{\mathrm{res}}(\mathbf{r})} | \mathrm{e}^{\mathrm{j}\Phi_{\mathrm{res}}(\mathbf{r})} \right\rangle_{\mathrm{P}} \langle \mathrm{M}_0(\mathbf{r}) | \mathrm{M}_0(\mathbf{r}) \rangle_{\mathrm{P}}}} \right|^2 \cdot \exp(-\sigma^2_{\mathrm{super-fitting}}), \tag{16}$$

where $\Phi_{\mathrm{res}}(\mathbf{r}) = \sum_{\mathrm{i}=2}^{\mathrm{N_{max}}} \langle \mathbf{\Phi_{res}} | \mathrm{Z_i} \rangle \mathrm{Z_i}$ is the residual phase onto the truncated Zernike polynomial basis. The term $\sigma^2_{\mathrm{super-fitting}} = 0.458(\mathrm{n_r}+1)^{-5/3} \left(\frac{\mathrm{D}}{\mathrm{r_0}}\right)^{5/3}$ [29] accounts for the phase non represented on the basis, where $\mathrm{n_r}$ is the radial order of the last Zernike polynomial of the representation. This result is a variation on the asymptotic development of Noll residual phase variance given in [26].

Finally, we assume to be in the weak perturbations regime. Thus, the log-amplitude contribution ρ_{χ} can be approximated to the scintillation averaged over the aperture as in [18], also known as power in the bucket (PIB), multiplied by a constant penalty factor $\mathrm{e}^{-\sigma^2_{\chi}}$ [30,31], assessing for the mean coupling losses due to the log-amplitude spatial fluctuations over the aperture:

$$\rho_{\chi} = \mathrm{PIB} \cdot \mathrm{e}^{-\sigma^2_{\chi}} = \iint |\Psi(\mathbf{r})|^2 \, \mathrm{P}(\mathbf{r}) \mathrm{d}^2\mathrm{r} \cdot \mathrm{e}^{-\sigma^2_{\chi}}. \tag{17}$$

At this stage, there is no assumption made about the statistics of neither ρ_{Φ} nor ρ_{χ}.

2.4.3. Pseudo-analytical modeling

We call pseudo-analytical modeling the approach relying on the generation of random complex fields thanks to analytical formulas, that are then coupled to a gaussian mode through a numerical overlap integral. The method to model the statistic of the phase of the complex field can vary. Fourier approaches are adopted in [19]. We choose the modal approach as in [7,18,32]. However, with respect to the former modal method that considers only the diagonal of the covariance matrix, we developed a formalism that is general to every AO correction linear with the AO measurements which considers the cross-correlations between the modes that are shown to be non negligible in the classical pre-compensation case [33].

To apply this pseudo-analytical formalism, we assume that Γ_{res} is known. For instance, in the classical pre-compensation case, its residual phase covariance matrix from Eq. (12) requires only to compute the phase angular modal covariance which can be found in [34]. These covariance matrix terms can be calculated thanks to the OGS and atmospheric parameters, in particular the $\mathrm{C_n^2}$ profile that is supposed to be known, which gives the distribution of the turbulence strength along the line of sight. Then, knowing the statistics of the residual phase, whose Zernike projections follow a centered normal distribution [35] given by $\mathbf{\Gamma_{res}}$, one can make an arbitrary

Optics EXPRESS

large number of residual phases draws, synthesize complex fields and compute the numerical overlap integral mentioned above to obtain the coupling phase contribution. These draws are made in the diagonalized space of the covariance matrix to account for the cross-correlations.

Finally, the PIB contribution from Eq. (17) can be expressed as $e^{2\chi_{Ap}}$, where the aperture-averaged log-amplitude χ_{Ap} follows a normal distribution [18] of variance $\sigma^2_{\chi_{Ap}}$ and mean $-\sigma^2_{\chi_{Ap}}$ to ensure energy conservation with $\mathbb{E}[e^{2\chi_{Ap}}] = 1$. Therefore, ρ_χ follows a log-normal distribution. In the same way, one can therefore draw samples from this law.

3. Minimum mean square error phase estimation

3.1. General MMSE method

Here, we aim to optimize the AO correction phase $\hat{\mathbf{\Phi}}_{\mathbf{AO,PAA}}$ and compute the associated residual phase covariance matrix $\mathbf{\Gamma}_{AO,res}$. To this end, we use a minimum mean square error (MMSE) method [36] to minimize the residual phase variance. For normal distributed random vectors, the estimator is linear and the reconstructor $\mathbf{R}$ is given by:

$$\mathbf{R}_{MMSE} \triangleq \text{argmin}_{\mathbf{R}} \text{tr}(\mathbf{\Gamma}_{AO,res}) = \mathbf{\Gamma}_{\Phi y_m}(\alpha_{PAA})\mathbf{\Gamma}_{y_m y_m}(0)^{-1} \tag{18}$$

and the theoretical associated covariance matrix is, applying Eq. (11):

$$\mathbf{\Gamma}_{AO,res-MMSE} = \mathbf{\Gamma}_{\Phi\Phi}(0) - \mathbf{R}_{MMSE}\mathbf{\Gamma}_{\Phi y_m}(\alpha_{PAA})^T. \tag{19}$$

In the above developments, the statistical priors correspond to the knowledge of the covariance matrices $\mathbf{\Gamma}_{\Phi y_m}(\alpha_{PAA})$ and $\mathbf{\Gamma}_{y_m y_m}(0)$.

3.2. Estimator based on phase measurements and priors

The MMSE estimation has been used in [20] for astronomical applications by using:

$$\mathbf{y}_m = [\mathbf{\Phi}_0], \tag{20}$$

where $\mathbf{\Phi}_0 \in \mathbb{R}^{N_{AO}-1}$ is the on-axis phase measurements.

We compute the MMSE estimator $\mathbf{R}_{MMSE_\Phi}$ as in Eq. (18). The two covariance matrices of the estimator can be developed as the matrices below:

$$\mathbf{\Gamma}_{\Phi y_m}(\alpha_{PAA}) = \mathbf{\Gamma}_{\Phi\Phi}(\alpha_{PAA}) \tag{21}$$

and,

$$\mathbf{\Gamma}_{y_m y_m}(0) = \mathbf{\Gamma}_{\Phi\Phi}(0) \tag{22}$$

By applying Eq. (19), its residual phase covariance matrix is then:

$$\mathbf{\Gamma}_{AO,res-MMSE_\Phi} = \mathbf{\Gamma}_{\Phi\Phi}(0) - \mathbf{R}_{MMSE,\Phi}\mathbf{\Gamma}_{\Phi\Phi}(\alpha_{PAA})^T. \tag{23}$$

The performance of this estimator will be computed and compared to the one of the other methods in section 4.

3.3. Proposed estimator based on phase and log-amplitude measurements and priors

We propose an MMSE estimator based on a measurement of the phase and the log-amplitude and the associated statistical priors. Indeed, the log-amplitude of the complex field still carry information about perturbations occurring in the atmosphere upper layers, where the downlink and uplink beam footprints are the more separated. Adding the log-amplitude information to

Optics EXPRESS

the phase estimation can thus bring information about the phase perturbations at the origin of anisoplanatism. We define the new measurement vector as the following block matrix:

$$\mathbf{y}_{\mathrm{m}} = \begin{pmatrix} \boldsymbol{\Phi}_0^{\mathrm{T}} & \boldsymbol{\chi}_0^{\mathrm{T}} \end{pmatrix}^{\mathrm{T}}, \tag{24}$$

where $\mathbf{y}_{\mathrm{m}} \in \mathbb{R}^{2N_{\mathrm{AO}}-1}$.

We compute the MMSE estimator $\mathbf{R}_{\mathrm{MMSE}_{\Phi\chi}}$ as in Eq. (18). The two covariance matrices of the estimator can be developed as the block matrices below:

$$\boldsymbol{\Gamma}_{\Phi \mathrm{y}_{\mathrm{m}}}(\alpha_{\mathrm{PAA}}) = \begin{bmatrix} \boldsymbol{\Gamma}_{\Phi\Phi}(\alpha_{\mathrm{PAA}}) & \boldsymbol{\Gamma}_{\Phi\chi}(\alpha_{\mathrm{PAA}}) \end{bmatrix} \tag{25}$$

and,

$$\boldsymbol{\Gamma}_{\mathrm{y}_{\mathrm{m}}\mathrm{y}_{\mathrm{m}}}(0) = \begin{bmatrix} \boldsymbol{\Gamma}_{\Phi\Phi}(0) & \boldsymbol{\Gamma}_{\Phi\chi}(0) \\ \boldsymbol{\Gamma}_{\Phi\chi}(0)^{\mathrm{T}} & \boldsymbol{\Gamma}_{\chi\chi}(0) \end{bmatrix} \tag{26}$$

As in Eq. (19), the theoretical associated covariance matrix in this case can be given by:

$$\boldsymbol{\Gamma}_{\mathrm{AO,res-MMSE}_{\Phi\chi}} = \boldsymbol{\Gamma}_{\Phi\Phi}(0) - \mathbf{R}_{\mathrm{MMSE}_{\Phi\chi}} \boldsymbol{\Gamma}_{\Phi \mathrm{y}_{\mathrm{m}}}(\alpha_{\mathrm{PAA}})^{\mathrm{T}}. \tag{27}$$

3.4. Analytical terms of the covariance matrices

The phase and the log-amplitude of the two fields are expressed as vectors in the modal formalism, we can therefore define the angular covariance matrices in the telescope pupil under the notations of section 2.1 as:

$$\boldsymbol{\Gamma}_{\Phi\Phi}(\alpha_{\mathrm{PAA}}) \triangleq \left(\mathbb{E}[\mathrm{a}_{\mathrm{i}}^{0} \mathrm{a}_{\mathrm{j}}^{\alpha_{\mathrm{PAA}}}] - \mathbb{E}[\mathrm{a}_{\mathrm{i}}^{0}]\mathbb{E}[\mathrm{a}_{\mathrm{j}}^{\alpha_{\mathrm{PAA}}}] \right)_{2 \le \mathrm{i,j} \le N_{\mathrm{AO}}} \tag{28}$$

$$\boldsymbol{\Gamma}_{\chi\chi}(\alpha_{\mathrm{PAA}}) \triangleq \left(\mathbb{E}[\mathrm{b}_{\mathrm{i}}^{0} \mathrm{b}_{\mathrm{j}}^{\alpha_{\mathrm{PAA}}}] - \mathbb{E}[\mathrm{b}_{\mathrm{i}}^{0}]\mathbb{E}[\mathrm{b}_{\mathrm{j}}^{\alpha_{\mathrm{PAA}}}] \right)_{1 \le \mathrm{i,j} \le N_{\mathrm{AO}}} \tag{29}$$

$$\boldsymbol{\Gamma}_{\Phi\chi}(\alpha_{\mathrm{PAA}}) \triangleq \left(\mathbb{E}[\mathrm{a}_{\mathrm{i}}^{0} \mathrm{b}_{\mathrm{j}}^{\alpha_{\mathrm{PAA}}}] - \mathbb{E}[\mathrm{a}_{\mathrm{i}}^{0}]\mathbb{E}[\mathrm{b}_{\mathrm{j}}^{\alpha_{\mathrm{PAA}}}] \right)_{2 \le \mathrm{i} \le N_{\mathrm{AO}}, 1 \le \mathrm{j} \le N_{\mathrm{AO}}} \tag{30}$$

Let's note that all phase projection distributions are by definition centered, whereas this is not the case for the distribution of the first projection of the log-amplitude b_1 which mean is equal to the variance of the log-amplitude averaged by the pupil as explained in section 2.4.3. In the following, we assume knowing $\mathbb{E}[\mathrm{b}_1^{\alpha}]$ from past measurements allowing to compute the error on a centered measurement vector.

The modal angular covariance matrix of the phase was developed in [34], although neglecting the term related to Fresnel diffraction. Similarly, the log-amplitude covariance matrix ($\Delta\alpha = 0$) was derived in [27]. We extended and generalized these formulas to derive the angular covariance matrices between the three combinations of phase and log-amplitude. We assume in the following developments to be in the weak perturbations regime. We only consider the case of the covariance of beams co-located in the same telescope aperture as depicted in Fig. 2. We denote the matrix coefficients as $(\mathrm{x}, \mathrm{y}) \in \{(\mathrm{a}, \mathrm{a}), (\mathrm{a}, \mathrm{b}), (\mathrm{b}, \mathrm{b})\}$:

$$\begin{aligned} \mathbb{E}[\mathrm{x}_{\mathrm{i}}^{0} \mathrm{y}_{\mathrm{j}}^{\alpha_{\mathrm{PAA}}}] - \mathbb{E}[\mathrm{x}_{\mathrm{i}}^{0}]\mathbb{E}[\mathrm{y}_{\mathrm{j}}^{\alpha_{\mathrm{PAA}}}] = & 5.20 \mathrm{K}_{\mathrm{ij}} \int_0^{\mathrm{L}} \mathrm{dz} \mathrm{C}_{\mathrm{n}}^{2}(\mathrm{z}) \int_0^{+\infty} \mathrm{dk} \mathrm{k}^{\frac{-14}{3}} \\ & \mathrm{J}_{\mathrm{n_i}+1}(\mathrm{k}) \mathrm{J}_{\mathrm{n_j}+1}(\mathrm{k}) \mathrm{F}_{\mathrm{xy}}\left(\frac{\mathrm{zk}^2}{2\mathrm{k}_0 \mathrm{R}_{\mathrm{tel}}^2}\right)\left(1 + \frac{2\pi \mathrm{R}_{\mathrm{tel}}}{\mathrm{L}_0 \mathrm{k}}^2\right)^{\frac{-11}{6}} \cdot \\ & \left(\mathrm{S1} \cdot \mathrm{J}_{\mathrm{m_1}+\mathrm{m_2}}\left(\frac{\mathrm{kd}(\mathrm{z}, \Delta\alpha)}{\mathrm{R}_{\mathrm{tel}}}\right) + \mathrm{S2} \cdot \mathrm{J}_{|\mathrm{m_1}-\mathrm{m_2}|}\left(\frac{\mathrm{kd}(\mathrm{z}, \Delta\alpha)}{\mathrm{R}_{\mathrm{tel}}}\right)\right) \end{aligned} \tag{31}$$

where $(\mathrm{n_i}, \mathrm{m_i}), (\mathrm{n_j}, \mathrm{m_j})$ are the radial and azimuthal degrees of the ith and jth Zernike polynomials respectively, z is the distance to the OGS pupil on the line of sight, $\mathrm{R}_{\mathrm{tel}}$ is the aperture radius and

Optics EXPRESS

$k_0 = \frac{2\pi}{\lambda}$ is the wave number. K_{ij} is defined as $K_{ij} = \sqrt{(n_i+1)(n_j+1)}(-1)^{\frac{n_i+n_j-m_i-m_j}{2}} R_{tel}^{\frac{5}{3}} k_0^2$, $C_n^2(z)$ is the turbulence refractive index structure function at the distance to the pupil z, $J_n(k)$ are the Bessel functions of the first kind of order n. F_{xy} is the Fresnel term discriminating the physical quantities:

$$\begin{aligned} F_{xy} &: k \mapsto \cos^2(k) \quad \text{for (x,y) = (a,a), corresponding to } \mathbf{\Gamma}_{\Phi\Phi}(\Delta\alpha) \\ F_{xy} &: k \mapsto \sin^2(k) \quad \text{for (x,y) = (b,b), corresponding to } \mathbf{\Gamma}_{\chi\chi}(\Delta\alpha) \\ F_{xy} &: k \mapsto \sin(k)\cos(k) \quad \text{for (x,y) = (a,b), corresponding to } \mathbf{\Gamma}_{\Phi\chi}(\Delta\alpha), \end{aligned} \tag{32}$$

where $k = 2\pi f$ is the angular frequency. Moreover, $(1 + \frac{2\pi R_{tel}}{L_0 k}^2)^{\frac{-11}{6}}$ is the Von Karman term accounting for the turbulence outer scale L_0. The last part of the equation is the contribution of the angular correlation between the two beam footprints at a given height distant from $d(z, \Delta\alpha) = \Delta\alpha \cdot z$, where $\Delta\alpha$ is an oriented angle. S1 and S2 are the geometrical coefficients depicting the relative orientation of the beam footprints that can be found in [37,38].

4. Numerical results

4.1. System specifications

4.1.1. OGS and AO parameters

Throughout this study, we consider the OGS parameters presented in Table 1. We choose a unique configuration of interest rather than performing a parametric study.

Table 1. OGS and AO general parameters.

OGS Parameters	
Elevation	30°
α_{PAA}	18.5 μrad
λ	1550 nm
$D_{telescope}$	60 cm
AO Parameters	
N_{AO}	136

This configuration is characterized by a large aperture that limits the geometrical losses induced by the beam divergence, but results in increased wavefront perturbations in the telescope aperture, and thus requires a good quality AO system [7]. As a result, we set a 60 cm diameter which is in accordance with the current OGS designs [39–41]. In this scheme, the anisoplanatic error due to the angular decorrelation of the turbulence is larger, thus there is a greater interest in improving the correction at PAA. We consider a Feeder-link with a GEO satellite at 30° elevation corresponding to a point-ahead angle of 18.5 μrad. It is a plausible scenario for a link between a GEO satellite and an OGS in Europe [42]. The considered wavelength is 1550 nm to benefit from off-the-shelf telecom components and of low atmospheric attenuation. Concerning the AO parameters, we consider a high quality correction with a number of correction modes as high as $N_{AO} = 136$ (nr=15), in accordance with current OGS AO systems [40,43,44].

4.1.2. Atmospheric conditions

We consider statistically representative atmospheric C_n^2 profiles. These profiles, called MOSPAR-XY, are composite profiles constructed thanks to astronomical site measurement databases [45,46]. The construction of these profiles is detailed in [15,17]. X and Y are thresholds on the statistical

Optics EXPRESS

distributions of the anisoplanatic angle θ_0, describing the turbulence angular decorrelation, and the Fried parameter r_0, corresponding to the strength of the phase perturbation. For example, the MOSPAR-9090 is a profile whose θ_0 is chosen $P(x>\theta_0) = 0.9$ and r_0 is chosen $P(y>r_0) = 0.9$ according to on-site measurements.

To illustrate and evaluate the performance of the estimator, we choose a strong perturbation case MOSPAR-9090 as depicted in Fig. 3. We also explore a set of different strengths of r_0 and θ_0 with all combinations of thresholds $(X,Y) \in \{50, 60, 70, 80, 90\} \times \{50, 60, 70, 80, 90\}$. An example of the explored integrated parameters values with respect to their XY thresholds applied in the profile construction are given in Table 2. We precise that at fixed threshold X, respectively Y, the value of θ_0, respectively r_0, barely varies.

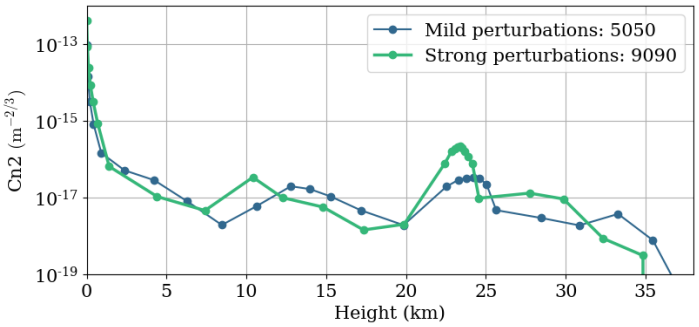

Fig. 3. Example of MOSPAR 5050 (blue) and MOSPAR 9090 (green) C_n^2 profile. The associated integrated parameters are $r_0 = 7.86$ cm and $r_0 = 4.03$ cm, $\theta_0 = 11.34$ µrad and $\theta_0 = 6.83$ µrad, $\sigma_\chi^2 = 0.04$ and $\sigma_\chi^2 = 0.08$, respectively.

Table 2. Table of the integrated parameters for different XY thresholds considered in the construction of a C_n^2 profile computed for a wavelength of 1550 nm and for a 30° elevation.

Parameter Threshold	5050	6060	7070	8080	9090
r_0 (cm)	7.8	6.8	5.8	4.9	4.1
θ_0 (µrad)	11.3	10.2	9.2	8.2	6.8
σ_χ^2	0.035	0.043	0.046	0.060	0.080

As the outer scale parameter impacts the low order Zernike mode variances which are supposed to induce the fades, we take it finite and explore the gain of the estimator for several $L_0 \in \{1, 2.15, 4.6, 10, 21.5, 46.4, 100, 215\}$ m. Furthermore, we assume the inner scale l_0 to be equal to zero.

4.2. Estimator performance

4.2.1. Case study

We analyse and compare the residual phase variance given by the classical pre-compensation from section 2.4, the MMSE phase from section 3.2 ($MMSE_\Phi$) and the new MMSE phase and amplitude from section 3.3 ($MMSE_{\Phi_\chi}$) methods on the strong perturbation case MOSPAR 9090 with an outer scale of 20 m, a typical value from the literature [47]. In Fig. 4, we plot the modal MSE ie. the modal residual phase variance on the AO subset as a function of the mode order. We can see that the $MMSE_\Phi$ brings negligible improvement compared to the classical method which suffers from the anisoplanatism error on all the modes. We also observe that the estimator

Optics EXPRESS

$\text{MMSE}_{\Phi\chi}$ brings an important reduction of the low order mode variances as highlighted in the red rectangle. We quantify the MSE reduction as $100 \cdot \left(1 - \frac{\text{MSE}(\Phi_{\text{res,MMSE}_{\Phi\chi}})}{\text{MSE}(\Phi_{\text{res,classic}})}\right)$. The total MSE is reduced of 47% while it even reaches 49% when considering only the tip and tilt modes respectively. We will show in the following that the reduction of these two modes is crucial to improve the statistic of the coupled flux.

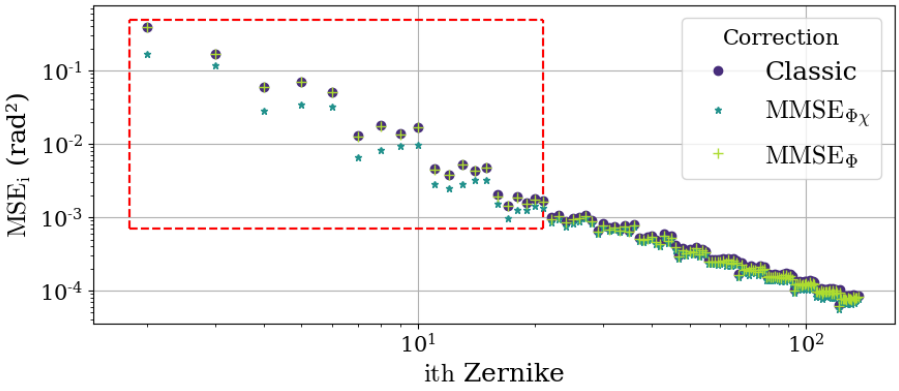

Fig. 4. Modal MSE evaluated for the three methods: the classical pre-compensation (blue dots), the MMSE phase (green crosses) and the MMSE phase and log-amplitude (blue stars). The performance is evaluated on the MOSPAR 9090 C_n^2 profile, with a fixed L0 of 20m.

Thanks to the pseudo-analytical model depicted in section 2.4.3, we generate 150000 independent samples of coupled flux for each phase correction case (classical, MMSE_{Φ} and $\text{MMSE}_{\Phi\chi}$). In Fig. 5(a) and Fig. 5(b) we plot the probability density function (PDF) as well as the cumulative density function (CDF) also known as fading probability [48], respectively, for each correction case. As expected, the PDF and CDF of the classical pre-compensation is superposed to the MMSE_{Φ} one (as they have almost the same phase statistics). We observe in Fig. 5(a) that the pdf associated to the $\text{MMSE}_{\Phi\chi}$ method shows higher mean value and smaller variance (with a scintillation index of 0.17 for the classic case and 0.06 for the $\text{MMSE}_{\Phi\chi}$). Moreover, the tail of the distribution is highly reduced. In Fig. 5(b), the tail reduction is highlighted with a 15 dB gain at probability 10^{-3} provided by the $\text{MMSE}_{\Phi\chi}$ with respect to the classical and MMSE_{Φ}. This threshold for fading probability is taken as a reference as explained in [49].

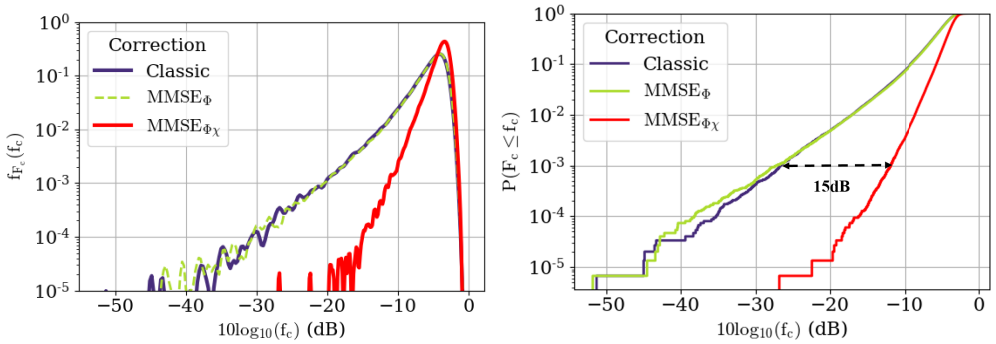

(a) Probability density function

(b) Cumulative density function

Fig. 5. Coupled flux statistics for MOSPAR 9090 at 30° elevation and L0=20m. The three correction cases are depicted: classic in dark blue, MMSE_{Φ} in green dots, $\text{MMSE}_{\Phi\chi}$ in red.

Optics EXPRESS

To summarize, we observe that the proposed estimator brings a gain on the low order modes of the residual phase variance and an improved coupled flux statistics. However, in this analysis, the contribution of all the modes is mixed in the coupled flux generation process. To evaluate the impact of some group of modes on the coupling statistics, we compare the classical correction case with a modified $\mathrm{MMSE}_{\Phi\chi}$ case. The modified case is constructed with a composite covariance matrix including the classic modal MSE from modes 2 to i and the $\mathrm{MMSE}_{\Phi\chi}$ error on modes i+1 to N_{AO}, in order to evaluate the impact of energetic low order modes. We study this two particular cases:

- Case A: Classic MSE on the group of mode of radial order 1 - $\mathrm{MMSE}_{\Phi\chi}$ from Z4 to 136,
- Case B: Classic MSE on the group of mode of radial order 1 and 2 - $\mathrm{MMSE}_{\Phi\chi}$ from Z7 to 136.

We observe in Fig. 6 that in both modified cases A and B, the high order corrected modes bring only a small improvement to the coupling statistics. In Fig. 6(a), the distribution of the A and B cases is slightly improved in mean and variance compared to the classical case. In Fig. 6(b), the CDFs of the A and B cases show only a 3 dB gain compared to the classical case. However, the slope of cases A and B are similar to the classical one, which is less steeper than the full $\mathrm{MMSE}_{\Phi\chi}$ corrected case. This means that deeper fades are far less likely with the new MMSE estimator. We conclude from these results that the tip-tilt MSE reduction has a strong impact on the signal distribution shape and on the CDF curve steepening and thus is a key metric to optimise. This was an expected result as the tip and tilt errors can be interpreted as a mispointing error induced by the turbulence in the plane of the satellite, or so called beam wander [50].

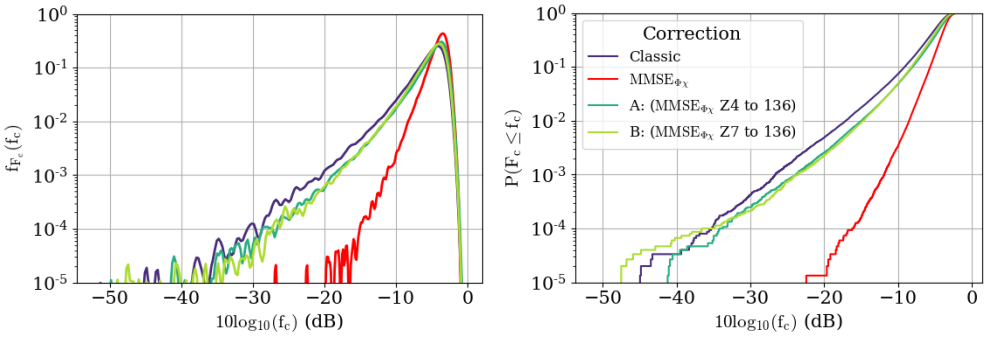

(a) Probability density function

(b) Cumulative density function

Fig. 6. Statistics of the coupled flux (CDF on the left, PDF on the right) when the gain on the tip and the tilt is cancelled (dark green), and when the gain on the modes from Z2 to 26 (light green) is cancelled. The statistics are compared with full classical error (dark blue) and full $\mathrm{MMSE}_{\Phi\chi}$ correction.

We also evaluate the estimator gain on the theoretical fundamental transmission limit of the channel by computing the outage probability. Indeed, the second Shannon theorem [51] stipulates that if the communication rate of the transmission is below the channel capacity (the theoretical upper bound of the rate that can be communicated for a given signal to noise ratio (SNR)), the communication can be error free. For a fading channel, the channel capacity is a random variable depending on the variable SNR function of the coupled flux. Thus, there is a non-zero probability that the channel capacity drops below the fixed rate r. When this happens, the communication

Optics EXPRESS

experiences an outage. The outage probability is:

$$P_{Outage} = P(r>C(SNR(f_c))) \text{ with } C(SNR(f_c)) = \log_2(1 + SNR(f_c)) = \log_2\left(1 + \frac{f_c}{N_0}\right), \quad (33)$$

where N_0 is the noise power and r the rate in bits per channel use (cu).

In Fig. 7, we plot the outage probability as a function of the SNR (dB) for a fixed rate of 2 bits/cu. It is used to consider the gain on the outage at probability 10^{-3} which is the forward error correction (FEC) coding limit [52]. This means that at this outage probability, the FEC is able to reduce after correction the error probability below 10^{-7}. We observe 15 dB gain on the outage probability for the proposed estimator compared to the classical method.

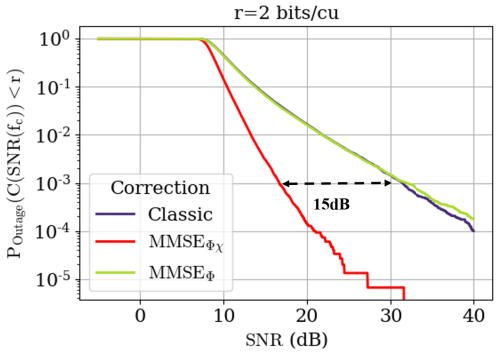

Fig. 7. Outage probability function of the SNR with a rate r=2bit/cu for the three correction methods (black for the classic, green for the $MMSE_{\Phi}$ method, red for the new $MMSE_{\Phi\chi}$ method). The gain at 10^{-3} is also highlighted.

With respect to these results, the estimator significant gain could allow to reconsider the use of large aperture telescopes by reducing the impact of atmospheric turbulence on the uplink coupled signal. This could allow to take advantage of the low beam divergence of large waist laser beams [7], while only adding software complexity and not hardware complexity at the OGS.

4.2.2. Robustness of the estimator to various atmospheric conditions

To assess the robustness of the estimator, we analyse its MSE and power reduction in several atmospheric turbulence scenarios. First we study the impact of the outer scale L_0 for a fixed C_n^2 profile, then we study all the MOSPAR profiles described in section 4.1.2 and Table 2 at fixed L_0.

In Fig. 8(a) and Fig. 8(b), we plot the total MSE and the Tip and Tilt MSE, respectively, as a function of L_0 for the MOSPAR 9090 case. We depict on both graphs several MSE reduction key points. We observe a saturation of the absolute MSE for both correction methods around L_0=10 m. The reduction rate reaches 46.6% for the total MSE and 49.4% for the tip and tilt MSE around L_0=20 m, which is a typical value considered in the literature. We can conclude that the proposed estimator provides a significant MSE reduction for all the outer scale considered values, with a greater reduction for large outer scales.

In Fig. 9, we plot the associated coupled flux CDF value at probability 10^{-3} in dB as a function of the outer scale as well as the gain brought by the proposed estimator. We can observe that this gain is comprised between 2.9 dB and 15.6 dB. Figure 8 and Fig. 9 also show that the outer scale strongly impact the phase and signal statistics. However, the proposed estimator, by limiting the increase of the phase MSE also shows to reduce the impact of L_0 on coupled flux statistics. This range, including the CDF value at probability 10^{-3} for an outer scale from 1 m to 200 m, is shown in Fig. 9 to be large of 8 dB for the proposed estimator whereas it is large of 20 dB concerning the classical method.

Optics EXPRESS

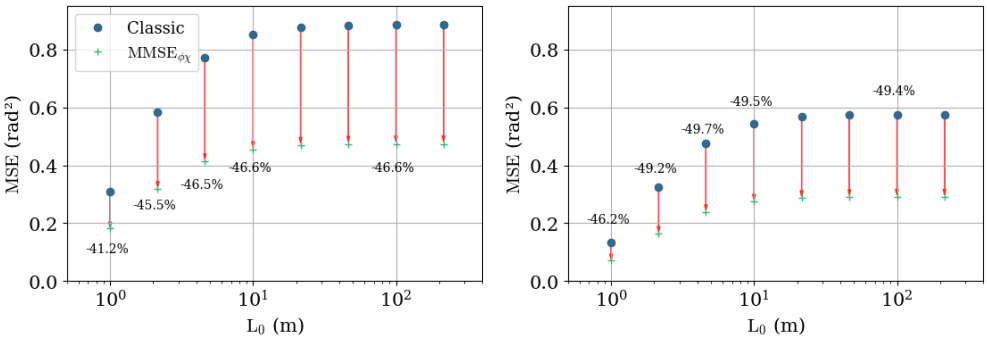

(a) Total MSE vs L_0.

(b) Tip and tilt MSE vs L_0.

Fig. 8. Absolute value of the MSE for the classical case (blue circles) and the MMSE$_{\Phi\chi}$ case (green crosses) versus L_0. Red arrows correspond to the MSE reduction provided by the MMSE$_{\Phi\chi}$ method, with the gain value below the arrow.(a) Total MSE error over the AO corrected modes, (b) MSE error on tip and tilt.

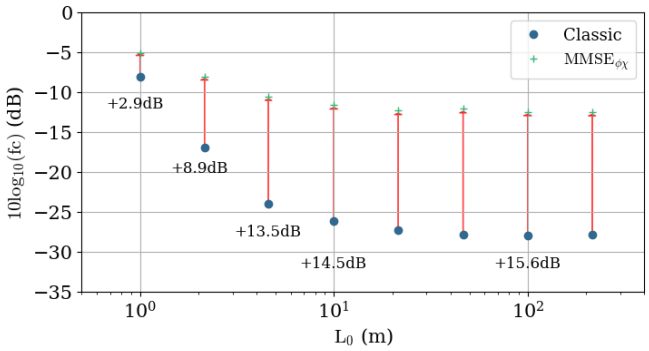

Fig. 9. Absolute value of the CDF at $P(f_c \leq F_c) = 10^{-3}$ for the classical case (blue circles) and the MMSE$_{\Phi\chi}$ case (green crosses) versus L_0. Red arrows correspond to the gain at probability 10^{-3} on the CDF provided by the MMSE$_{\Phi\chi}$ method, with the gain value given below the arrow.

Furthermore, we study the sensitivity to the C_n^2 profile. We set L_0 to its earlier value of 20 m In Fig. 10, we plot the MSE reduction gain as a function of θ_0, for different values of r_0.

In Fig. 10(a) and Fig. 10(b) we plot the total MSE and tip and tilt MSE, respectively, as a function of the anisoplanatic angle corresponding to the studied C_n^2 profile for different r_0 parameters. The results from the classical method and proposed estimator are represented by dots and crosses, respectively. The different colors depicts the different strengths of r_0. We observe that the total MSE value is almost independent from r_0. This was an expected result as the anisoplanatic error is mainly driven by θ_0. The total MSE is reduced from 35 to 46% and the tip-tilt MSE from 38 to 49%. We can conclude that, stronger is the anisoplanatism, larger is the gain. Additionally, we notice a higher gain than expected for the case MOSPAR 5050. This can be interpreted by the fact that the estimator gain depends also on the C_n^2 profile structure and not only on the parameter θ_0.

In Fig. 11, we plot the associated coupled flux threshold of the CDF at probability 10^{-3} as a function of the anisoplanatic angle corresponding to the considered C_n^2 profile. Similarly, we observe a quasi-null impact of the Fried parameter on the coupling attenuation value in both

Optics EXPRESS

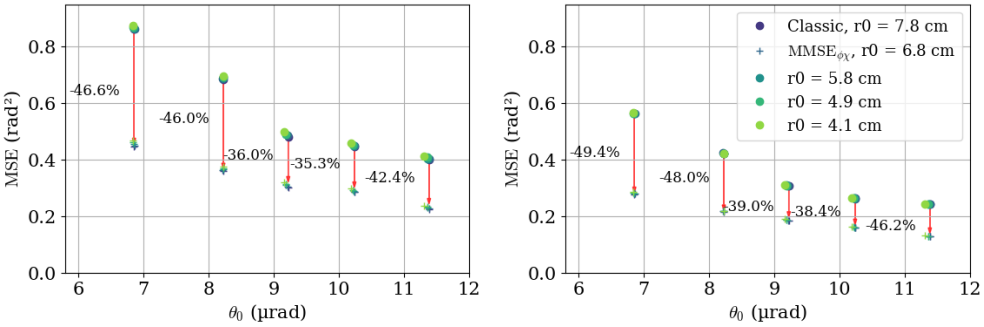

(a) Total MSE vs θ_0

(b) Tip and tilt MSE vs θ_0

Fig. 10. Absolute value of the MSE for the classical case (circles) and the $\text{MMSE}_{\Phi\chi}$ case (crosses) versus θ_0, for different r_0. Each color depicts a different r_0. Red arrows correspond to the MSE reduction provided by the $\text{MMSE}_{\Phi\chi}$ method, with the reduction value on its left. (a) Total MSE error over the AO corrected modes.(b) MSE error on tip and tilt.

classical and $\text{MMSE}_{\Phi\chi}$ cases. We observe a gain from 5.5 to 15.8 dB provided by the new estimator. Thus, we can conclude that the estimator gain (in phase variance or in coupled flux), is almost insensitive to r_0, and increases with more severe anisoplanatic conditions.

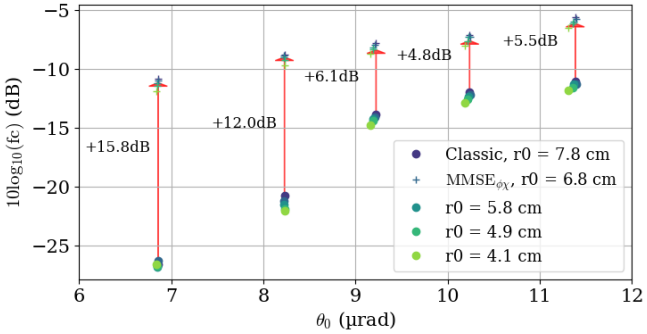

Fig. 11. Absolute value of the CDF at $P(f_c \leq F_c) = 10^{-3}$ for the classical case (circles) and the $\text{MMSE}_{\Phi\chi}$ case (crosses) versus θ_0. Each color depicts a different r_0. Red arrows corresponds to the gain at probability 10^{-3} on the CDF provided by the $\text{MMSE}_{\Phi\chi}$ method, with the gain given on the left of the arrow.

5. Conclusion and perspectives

In this article, we studied the coupled flux attenuation induced by the turbulence of an AO assisted ground to GEO satellite optical link suffering from anisoplanatism. This effect is due to the inherent point-ahead angle between the probed downlink and emitted uplink path directions and greatly impairs the quality of the AO correction.

We propose a new analytical MMSE phase estimator of the phase at PAA based on phase and log-amplitude downlink on-axis measurements and statistical priors. We derive a reciprocal analytical formalism to compute the estimator and extended the formulas from the literature to obtain the modal phase and log-amplitude angular cross-covariance matrix. We show that the proposed estimator significantly decreases the mean square error of the anisoplanatic residual phase variance, especially on low order modes. This confirms that log-amplitude

Optics EXPRESS

measurements complements the phase measurements and brings information on the distribution of the turbulence along the line of sight, allowing estimation at point-ahead angle. Note that this phase and log-amplitude complementarity can be used also in C_n^2 profiling [53,54]. We show through numerical simulation that the estimator provides high dB gains on the associated coupled flux and consequently we observe a gain on the outage probability. We highlight that the tip-tilt estimation drives most of the gain on the coupled flux statistics. These estimator properties were quantified for various atmospheric conditions based on C_n^2 profiles constructed from measurement databases, and various outer scales. This gain on the coupled flux statistics will allow to relax the already severe power constraints on the link budget of the GEO-Feeder link. It can also renew the interest in the large diameter OGS designs by reducing the impact of atmospheric turbulence on the uplink coupled signal, therefore allowing to take advantage of the low geometrical losses due to the low beam divergence of large telescope apertures. Beyond that, reducing the coupled signal fluctuations, thus reducing the fading events, could pave the way toward the implementation of telecom architectures such as transparent ones, very sensitive to fading events, therefore allowing to reduce the system complexity onboard the satellite [55].

In this study, we furthermore propose a general modal formalism based on covariance matrices to compute the phase statistics for an arbitrary phase estimation linear with on-axis measurements.

However, the presented results correspond to an ultimate performance on a idealized AO system. In practice, although dominated by the anisoplanatic error, the AO system suffers from additive errors such as the one induced by the AO loop delay. In future work, we will take into account this error in the residual phase covariance matrix but also as a prior in the equations. We will also study the temporal statistics of the resulting coupled flux and its impact on the telecom signal, especially on interleaver size. Furthermore, the results here were obtained with a known C_n^2 profile. Therefore, an additional perspective will be the assessment of the robustness of the estimator to C_n^2 profile uncertainties.

Funding. Centre National d'Etudes Spatiales; Office National d'études et de Recherches Aérospatiales.

Acknowledgments. We thank James Osborn (Centre for Advanced Instrumentation, Durham University) for kindly providing the turbulence profile data base described in [45]. We thank Laurie Paillier and Pablo Rodriguez-Robles for the fruitful scientific discussions and their support concerning the numerical simulations. We also thank Bouchra Benammar and Hugo Meric from CNES for their support and advice in the project development.

Disclosures. The authors declare no conflicts of interest.

Data availability. Data used to produce the article results are not publicly available but can be furnished by request to the author.

References

1. H. Hauschildt, C. Elia, H. L. Moeller, W. El-Dali, T. Navarro, M. Guta, S. Mezzasoma, and J. Perdigues, "Hydron: High throughput optical network," in *IEEE International Conference on Space Optical Systems and Applications*, (ICSOS, 2019), pp. 1–6.
2. H. Kaushal and G. Kaddoum, "Optical communication in space: Challenges and mitigation techniques," IEEE Commun. Surv. Tutorials **19**(1), 57–96 (2017).
3. C. Fuchs and F. Moll, "Ground station network optimization for space-to-ground optical communication links," J. Opt. Commun. Netw. **7**(12), 1148–1159 (2015).
4. I. I. Kim, H. Hakakha, P. Adhikari, E. J. Korevaar, and A. K. Majumdar, "Scintillation reduction using multiple transmitters," in *Free-Space Laser Communication Technologies IX*, vol. SPIE 2990, 102–113 (1997).
5. C. Fuchs, D. Giggenbach, R. M. Calvo, and W. Rosenkranz, "Transmitter diversity with phase-division applied to optical geo feeder links," IEEE Photonics Technol. Lett. **33**(11), 541–544 (2021).
6. H. Ordouei, M. Krzyzek, N. Perlot, and R. Freund, "Power and spectrum efficiencies of an optical satellite uplink with spatially diverse beams and incoherent combining," in *International Conference on Space Optics* (ICSO, 2020), vol. SPIE 11852, 118524H (2021).
7. J.-M. Conan, A. Montmerle-Bonnefois, N. Védrenne, C. B. Lim, C. Petit, V. Michau, M.-T. Velluet, J.-F. Sauvage, S. Meimon, C. Robert, J. Montri, F. Mendez, P. Perrault, G. Artaud, and B. Benammar, "Adaptive Optics for GEO-Feeder Links: from Performance Analysis via Reciprocity Based Models to Experimental Demonstration," in *Workshop Communications and Observations through Atmospheric Turbulence: characterization and mitigation (COAT)*, (2019).
8. R. K. Tyson, "Adaptive optics and ground-to-space laser communications," Appl. Opt. **35**(19), 3640–3646 (1996).

Optics EXPRESS

9. J. H. Shapiro, "Point-ahead limitation on reciprocity tracking," J. Opt. Soc. Am. **65**(1), 65–68 (1975).
10. J. Osborn, M. J. Townson, O. J. D. Farley, A. Reeves, and R. M. Calvo, "Adaptive optics pre-compensated laser uplink to leo and geo," Opt. Express **29**(4), 6113–6132 (2021).
11. F. Rigaut and E. Gendron, "Laser guide star in adaptive optics : the tilt determination problem," Astron. Astrophys. **261**, 677–684 (1992).
12. N. Védrenne, A. Montmerle-Bonnefois, C. B. Lim, C. Petit, J.-F. Sauvage, S. Meimon, P. Perrault, F. Mendez, B. Fleury, J. Montri, J.-M. Conan, V. Michau, Z. Sodnik, and C. Voland, "First experimental demonstration of adaptive optics pre-compensation for geo feeder links in a relevant environment," in *IEEE International Conference on Space Optical Systems and Applications*, (ICSOS, 2019), pp. 1–5.
13. A. Brady, C. Rössler, N. Leonhard, M. Gier, P. Böttner, R. Eberhardt, A. Tünnermann, and C. Reinlein, "Validation of pre-compensation under point-ahead-angle in a 1 km free-space propagation experiment," Opt. Express **27**(13), 17840–17850 (2019).
14. R. Saathof, R. den Breeje, W. Klop, N. Doelman, T. Moens, M. Gruber, T. Russchenberg, F. Pettazzi, J. Human, R. M. Calvo, J. Poliak, R. Barrios, M. Richerzhagen, and I. Ferrario, "Pre-correction adaptive optics performance for a 10 km laser link," in *Free-Space Laser Communications XXXI*, vol. SPIE 10910, 109101H (2019).
15. A. Montmerle-Bonnefois, M.-T. Velluet, M. Cissé, C. B. Lim, J.-M. Conan, C. Petit, J.-F. Sauvage, S. Meimon, P. Perrault, F. Mendez, B. Fleury, J. Montri, V. Michau, and N. Védrenne, "First feasibility demonstration of AO pre-compensation for GEO feeder links in a relevant environment," Opt. Express (2022). To be published.
16. N. Védrenne, J. Conan, M. Velluet, M. Sechaud, M. Toyoshima, H. Takenaka, A. Guérin, and F. Lacoste, "Turbulence effects on bi-directional ground-to-satellite laser communication systems," in *Proc. Int. Conf. Sp. Opt. Syst. Appl*, vol. 12 (2012).
17. N. Védrenne, C. Petit, A. Montmerle-Bonnefois, C. B. Lim, J.-M. Conan, L. Paillier, M.-T. Velluet, K. Caillault, F. Gustave, A. Durecu, V. Michau, F. Cassaing, S. Meimon, and J. Montri, "Performance analysis of an adaptive optics based optical feeder link ground station," in *International Conference on Space Optics — ICSO 2020*, vol. SPIE 11852, 1185219 (2021).
18. L. Canuet, N. Védrenne, J.-M. Conan, C. Petit, G. Artaud, A. Rissons, and J. Lacan, "Statistical properties of single-mode fiber coupling of satellite-to-ground laser links partially corrected by adaptive optics," J. Opt. Soc. Am. A **35**(1), 148–162 (2018).
19. O. J. D. Farley, M. J. Townson, and J. Osborn, "Fast: Fourier domain adaptive optics simulation tool for bidirectional ground-space optical links through atmospheric turbulence," Opt. Express **30**(13), 23050 (2022).
20. M. R. Whiteley, B. M. Welsh, and M. C. Roggemann, "Optimal modal wave-front compensation for anisoplanatism in adaptive optics," J. Opt. Soc. Am. A **15**(8), 2097 (1998).
21. B. Neichel, T. Fusco, and J.-M. Conan, "Tomographic reconstruction for wide-field adaptive optics systems: Fourier domain analysis and fundamental limitations," J. Opt. Soc. Am. A **26**(1), 219–235 (2009).
22. C. M. Correia, K. Jackson, J.-P. Véran, D. Andersen, O. Lardière, and C. Bradley, "Spatio-angular minimum-variance tomographic controller for multi-object adaptive-optics systems," Appl. Opt. **54**(17), 5281–5290 (2015).
23. J. H. Shapiro and A. L. Puryear, "Reciprocity-enhanced optical communication through atmospheric turbulence — Part I: Reciprocity proofs and far-field power transfer optimization," J. Opt. Commun. Netw. **4**(12), 947–954 (2012).
24. A. L. Puryear, J. H. Shapiro, and R. R. Parenti, "Reciprocity-enhanced optical communication through atmospheric turbulence - part II: communication architectures and performance," in *Laser Communication and Propagation through the Atmosphere and Oceans*, vol. SPIE 8517, 545–556 (2012).
25. C. Robert, J.-M. Conan, and P. Wolf, "Impact of turbulence on high-precision ground-satellite frequency transfer with two-way coherent optical links," Phys. Rev. A **93**(3), 033860 (2016).
26. R. J. Noll, "Zernike polynomials and atmospheric turbulence," J. Opt. Soc. Am. **66**(3), 207–211 (1976).
27. F. Mahé, V. Michau, G. Rousset, and J.-M. Conan, "Scintillation effects on wavefront sensing in the Rytov regime," in *Propagation and Imaging through the Atmosphere IV*, vol. SPIE 4125, 77–86 (2000).
28. N. Perlot, "Turbulence-induced fading probability in coherent optical communication through the atmosphere," Appl. Opt. **46**(29), 7218 (2007).
29. J.-M. Conan, "Etude de la correction partielle en optique adaptative," Ph.D. thesis, Paris 11 (1994).
30. F. Mahé, "Application d'un modèle atmosphérique à l'étude des fluctuations d'indice de réfraction dans la couche limite : influence de la scintillation sur l'analyse de front d'onde," Ph.D. thesis (2000).
31. R. J. Sasiela, "Basic equations for wave propagation in turbulence," in *Electromagnetic Wave Propagation in Turbulence*, (Springer, 1994), pp. 19–46.
32. N. Védrenne, J.-M. Conan, C. Petit, and V. Michau, "Adaptive optics for high data rate satellite to ground laser link," in *Free-Space Laser Communication and Atmospheric Propagation XXVIII*, vol. SPIE 9739, 97390E (2016).
33. P. Lognoné, J.-M. Conan, L. Paillier, N. Védrenne, and G. Rekaya, "Channel model of a ground to satellite optical link pre-compensated by adaptive optics," in *Signal Processing in Photonic Communications*, (Optica Publishing Group, 2022), pp. SpTu3G–3.
34. F. Chassat, "Theoretical evaluation of the isoplanatic patch of an adaptive optics system working through the atmospheric turbulence," J. Opt. **20**(1), 13–23 (1989).
35. F. Roddier, *Adaptive Optics in Astronomy* (Cambridge University Press, 1999).
36. S. M. Kay, *Fundamentals of statistical signal processing: estimation theory* (Prentice-Hall, Inc., 1993).

Optics EXPRESS

37. F. Chassat, "Optical propagation through atmospheric turbulence. Model analysis of anisoplanatism and application to adaptive optics," Ph.D. thesis, Office National d'Etudes et de Recherche Aerospatiale, France (1992).
38. A.-R. Camboulives, "Atmospheric turbulence effects mitigation for a ground to geostationary satellite optical link : impact on the ground terminal architecture," Ph.D. thesis, Université Paris Saclay (2017).
39. K. Mudge, B. Clare, E. Jager, V. Devrelis, F. Bennet, M. Copeland, N. Herrald, I. Price, G. Lechner, J. Kodithuwakkuge, J. Magarelli, D. Bandara, C. Peck, M. Hollick, P. Alvino, P. Camp-Smith, B. Szumylo, A. Raj, and K. Grant, "Dstg laser satellite communications -current activities and future outlook," in *IEEE International Conference on Space Optical Systems and Applications*, (ICSOS, 2022), pp. 17–21.
40. C. Petit, A. Montmerle-Bonnefois, J.-M. Conan, A. Durecu, F. Gustave, C. Lim, J. Montri, L. Paillier, P. Perrault, M.-T. Velluet, J.-B. Volatier, and N. Védrenne, "Feelings : the onera optical ground station for geo feeder links demonstration," in *IEEE International Conference on Space Optical Systems and Applications*, (ICSOS, 2022), pp. 255–260.
41. D. Kolev, K. Shiratama, A. Carrasco-Casado, Y. Saito, Y. Munemasa, J. Nakazono, P. V. Trinh, H. Kotake, H. Kunimori, T. Kubooka, T. Fuse, and M. Toyoshima, "Status update on laser communication activities in nict," in *IEEE International Conference on Space Optical Systems and Applications*, (ICSOS, 2022), pp. 36–39.
42. A. Mengali, C. I. Kourogiorgas, N. K. Lyras, B. Shankar Mysore Rama Rao, F. Kayhan, A. D. Panagopoulos, T. Bäumer, and K. Liolis, "Ground-to-geo optical feeder links for very high throughput satellite networks: Accent on diversity techniques," International Journal of Satellite Communications and Networking (2020).
43. Z. Sodnik, J. P. Armengol, R. H. Czichy, and R. Meyer, "Adaptive optics and ESA's optical ground station," in *Free-Space Laser Communications IX*, vol. SPIE 7464, 746406 (2009).
44. E. Fischer, T. Berkefeld, M. Feriencik, M. Feriencik, V. Kaltenbach, D. Soltau, B. Wandernoth, R. Czichy, J. Kunde, K. Saucke, F. Heine, M. Gregory, C. Seiter, and H. Kampfner, "Development, integration and test of a transportable adaptive optical ground station," in *IEEE International Conference on Space Optical Systems and Applications*, (ICSOS, 2015), pp. 1–6.
45. J. Osborn, R. W. Wilson, M. Sarazin, T. Butterley, A. Chacón, F. Derie, O. J. D. Farley, X. Haubois, D. Laidlaw, M. LeLouarn, E. Masciadri, J. Milli, J. Navarrete, and M. J. Townson, "Optical turbulence profiling with Stereo-SCIDAR for VLT and ELT," Mon. Not. R. Astron. Soc. **478**(1), 825–834 (2018).
46. D. Sprung and E. Sucher, "Characterization of optical turbulence at the solar observatory at the Mount Teide, Tenerife," in *Remote Sensing of Clouds and the Atmosphere XVIII; and Optics in Atmospheric Propagation and Adaptive Systems XVI*, vol. SPIE 8890, 889015 (2013).
47. A. Ziad, "Review of the outer scale of the atmospheric turbulence," in *Adaptive Optics Systems V*, vol. SPIE 9909, 99091K (2016).
48. R. Barrios and F. Dios, "Probability of fade and BER performance of FSO links over the exponentiated Weibull fading channel under aperture averaging," in *Unmanned/Unattended Sensors and Sensor Networks IX*, vol. SPIE 8540, 79–87 (2012).
49. H. Kotake, Y. Abe, M. Sekiguchi, T. Fuse, H. Tsuji, and M. Toyoshima, "Link budget design of adaptive optical satellite network for integrated non-terrestrial network," in *IEEE International Conference on Space Optical Systems and Applications*, (ICSOS, 2022), pp. 240–247.
50. R. Fante, "Electromagnetic beam propagation in turbulent media," Proc. IEEE **63**(12), 1669–1692 (1975).
51. C. E. Shannon, "Communication in the presence of noise," Proc. IRE **37**(1), 10–21 (1949).
52. A. Tychopoulos, O. Koufopavlou, and I. Tomkos, "Fec in optical communications - a tutorial overview on the evolution of architectures and the future prospects of outband and inband fec for optical communications," IEEE Circuits Devices Mag. **22**(6), 79–86 (2006).
53. N. Védrenne, V. Michau, C. Robert, and J.-M. Conan, "Cn2 profile measurement from shack-hartmann data," Opt. Lett. **32**(18), 2659–2661 (2007).
54. C. Sauvage, C. Robert, L. M. Mugnier, J.-M. Conan, J.-M. Cohard, K.-L. Nguyen, M. Irvine, and J.-P. Lagouarde, "Near ground horizontal high resolution cn2 profiling from shack–hartmann slopeand scintillation data," Appl. Opt. **60**(34), 10499–10519 (2021).
55. R. Mata Calvo, D. Giggenbach, A. Le Pera, J. Poliak, R. Barrios, and S. Dimitrov, "Optical feeder links for very high throughput satellites-system perspectives," in *KA and Broadband communication conference*, (2015).